



Power Electronic Systems
Laboratory

© 2019 IEEE

IEEE Transactions on Industrial Electronics, Vol. 66, No. 6, pp. 4880-4890, June 2019

Energy Harvesting with Single-Sided Linear Induction Machines Featuring Secondary Conductive Coating

M. Flankl,
A. Tüysüz,
L. de Oliveira Baumann,
J. W. Kolar

Personal use of this material is permitted. Permission from IEEE must be obtained for all other uses, in any current or future media, including reprinting/republishing this material for advertising or promotional purposes, creating new collective works, for resale or redistribution to servers or lists, or reuse of any copyrighted component of this work in other works.



Eidgenössische Technische Hochschule Zürich
Swiss Federal Institute of Technology Zurich

Energy Harvesting with Single-Sided Linear Induction Machines featuring Secondary Conductive Coating

Michael Flankl, *Student Member, IEEE*, Lucas de Oliveira Baumann, *Student Member, IEEE*, Arda Tüysüz, *Member, IEEE*, and Johann W. Kolar, *Fellow Member, IEEE*

Abstract—With the continuously broadening application area of Internet of Things (IoT), robust energy harvesters and power conditioning units for supplying remote sensors and actuators are gaining importance. A Single-Sided Linear Induction Machine (SLIM) with solid secondary operating in generator mode could meet these requirements as it can harvest electric energy from the kinetic energy of a moving conductive body (secondary). Therefore, the energy harvesting performance of SLIMs is studied in this work, using analytical models, which are derived with special attention to the case where a conductive coating is applied on the mover - a simple and practical modification that is shown to increase the harvester performance significantly. Measurements are given for three different secondary materials and stator geometries. It is shown that 15 W of electrical power can be harvested with 14% efficiency over an air gap of 0.5 mm from a copper-coated steel mover with a surface speed of 29 m/s, covering only 17 cm² of surface area.

Index Terms—Linear induction machine, solid rotor machine, SLIM, energy harvesting, IoT, inductive power transmission, steel, scaling law.

NOMENCLATURE

A_1	Stator current sheet
A_{slot}	Winding window (per coil side)
A_{wire}	Wire cross section
B_2	Secondary flux density
B_g	Air gap flux density
d_{coat}	Coating thickness
δ_2	Secondary skin depth
δ_{coat}	Skin depth in coating
g	Air gap
I_1, i_1	Stator phase current (RMS, $i(t)$)
I_2, i_2	Secondary current (RMS, $i(t)$)
$I_{\text{coat}}, i_{\text{coat}}$	Sec. coating current (RMS, $i(t)$)
I_m, i_m	Main inductance current (RMS, $i(t)$)
j_2	Secondary current density
j	Imaginary unit $\sqrt{-1}$
k	Power scaling factor
k_f	Copper filling factor
k_c	Carter factor
κ_{coat}	Coating conductivity

κ_{Cu}	Copper conductivity
κ_2	Secondary conductivity
l_{wire}	Generic wire length
l_x	Coil span
l_y	Stator width
l_{end}	End winding length
L_1	Stator stray inductance
L'_2	Secondary stray inductance
L_m	Main inductance
m	Number of phases
μ_2	Secondary apparent permeability
μ_{coat}	Coating permeability
N	Number of turns
p	Number of pole pairs
P_1	Primary electrical power (RMS)
P_2	Secondary extracted electrical power (RMS)
P_{cu}	Stator copper losses (RMS)
R_1	Stator winding resistance
R'_2	Secondary resistance
s	Slip
\vec{s}_B	Complex Eigenvalue for B_2 solution
S	RMS current density
τ	Pole pitch
Θ	Excitation field
u_1	Stator phase voltage
u_m	Main inductance voltage
v_2	Secondary surface speed
ξ	Winding factor
Z'_2	Secondary impedance
ω_1	Stator angular frequency
ω_2	Secondary angular frequency

I. INTRODUCTION

TODAY, the term energy harvesting (EH) is often associated with systems harvesting energy from ambient sources such as vibration, radiation and temperature gradients. The purpose of EH systems is to supply electric power, where no alternative besides a battery system is possible. Therefore, the energy efficiency of the EH transducer is not a primary concern. Power ratings of such systems typically range from a few microwatts [1], [2] to milliwatts [3], [4]. On the other hand, with the continuously broadening application area of Internet of Things (IoT), there is a growing need for local, robust, modular and low-cost power supplies capable of powering remote systems comprising various sensors, signal processors,

Manuscript received September 11, 2017; revised December 19, 2017 and February 20, 2018; accepted March 18, 2018. All authors are with the Power Electronic Systems Laboratory, Swiss Federal Institute of Technology, Zurich, 8092, Switzerland (e-mail: flankl@lem.ee.ethz.ch)

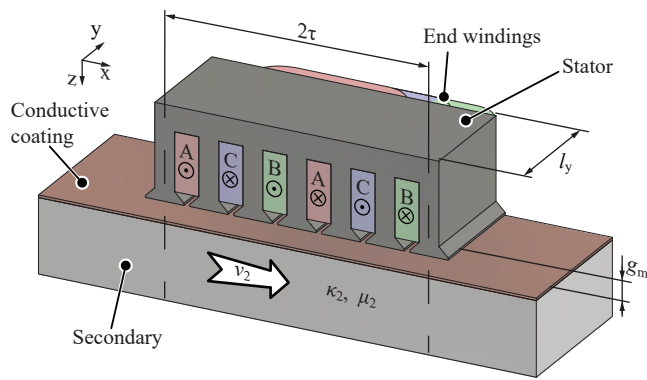


Fig. 1. Illustration of a SLIM utilized for energy harvesting (EH) with a solid secondary and a conductive (copper) coating.

wireless communication hardware, and even actuators [5]–[7]. The power demand of such remote systems may well be in the range of several watts.

Linear induction machines (LIMs) are commonly utilized in well-known motor applications such as traction in both low-speed [8], [9] and high-speed [10]–[13] ground transportation as well as for production machines [14] and flywheel energy storages [15]. As LIMs omit the use of permanent magnets, they are well suited for harsh surroundings and high temperatures. Another machine topology, which features these qualities is the solid rotor machine, where a circumferential stator, practically identical to that of a squirrel-cage rotating induction machine is combined with an unlaminated rotor made of solid steel, which might or might not be slitted and/or coated with a sleeve of non-ferromagnetic material. Combining the properties of LIMs and solid rotor machines result in the single-sided linear induction machine (SLIM) with solid rotor. It can simply be realized with a linear stator aligned in parallel to the moving body (henceforth be denoted as the secondary), which could be a short sector of a shaft or a linear moving system.

In this work, a robust, low-cost and high-power, i.e. watt-range, SLIM energy harvester is proposed. It harvests electrical energy from the kinetic energy of an electrically conductive body that is in motion and placed in the vicinity of a remote system to be supplied. This arrangement may have several practical applications; for instance the secondary could be a body in motion with respect to the SLIM stator (in which case the stator would have a linear shape, see Fig. 1), or a large-diameter shaft, which is partially covered by the SLIM stator (in which case the stator would be arc shaped).

Motoring operation of SLIMs is fairly well covered in literature [9]–[13], [16]. Initial considerations regarding EH operation are reported in [17]. However, (and as confirmed later) coating the secondary with a thin conductive layer can improve the performance in terms of harvested power and overall efficiency significantly. Therefore, the models presented in [17] are extended towards a scaling law for EH with a two-layered secondary. Moreover, selected measures to improve the SLIM's performance particularly in EH are addressed in this work. An optimal winding scheme for the required, comparably small linear stator is selected and

reactive power compensation to reduce the SLIM's apparent power demand is analyzed and discussed with measurements.

A brief overview on the electrical modeling of a SLIM is given in Sec. II and a scaling law for the EH operation is derived in Sec. III. Moreover, Sec. IV analyzes practical implications on the winding scheme, occurring in the design phase of a SLIM for EH. In Sec. V, FEM and measurement results for EH are presented. In Sec. VI, a compact prototype of a SLIM energy harvester is presented and possibilities for reactive power compensation are investigated. Finally, Sec. VII concludes the paper.

II. SYSTEM OVERVIEW AND MODELING

SLIMs and LIMs share the same working principle and main properties as a rotating induction machine. By cutting open the rotor and stator of a rotating induction machine, one can achieve a SLIM, where rotor and stator are parallel to each other and separated by an air gap (see Fig. 1). The stator is referred to as the primary as it is the source of excitation. Its three-phase winding system (see Fig. 1) generates a time-varying magnetic field, which is moving along the air gap. This is in analogy to the rotation of the field in a rotating (e.g. squirrel-cage induction) machine. The rotor (secondary) is moving with a surface speed v_2 (see Fig. 1). The SLIM topology analyzed for EH has a secondary, which is made of solid (unlaminated) conductive material, e.g. steel. The time-varying magnetic field created by the stator windings induces eddy currents in the conductive secondary. Due to interaction of the eddy currents and the magnetic field, Lorentz forces enable the electromechanical energy conversion. The EH is conducted with driving the SLIM in generative operation mode. Hence, a stationary observer would see the magnetic field in the air gap moving slower than the surface speed v_2 of the secondary.

Widely used, rotating squirrel-cage induction machines have a secondary with copper or aluminum bars placed in slots of a rotor core made of laminated iron. The conductive bars carry the induced currents and the laminated iron provides a path for the magnetic flux. On the other hand, solid-secondary induction machines utilize a solid (i.e. unlaminated) secondary (e.g. made of steel) to carry both the induced currents and the magnetic flux. As shown in literature [18], geometric modifications such as slitting the secondary improve the machine's performance. However, the idea of this paper is to harvest energy from an existing body with a smooth surface, which is moving with a sufficient surface speed. Therefore, major modifications of the secondary geometry, such as slitting are not possible and not further investigated. In the same spirit, commonly used materials in structural machine parts, namely steels C45E (Mat. No. 1.1191 cf. [19]), S235 (Mat. No. 1.0038 cf. [20]), and aluminum Ac-112 (Mat. No. 6082 cf. [21]) are considered as secondary material. On the other hand, coating the secondary surface with a thin layer of copper, which is reported to increase the performance of solid-secondary induction machines [22], would practically be applicable in many industrial settings. It is therefore analyzed in detail both analytically and experimentally in this paper. It is common practice to use an arc-shaped stator and a rotating, cylindrical secondary with a sufficiently large diameter for the experimental analysis of SLIMs [23]–[26] and therefore the

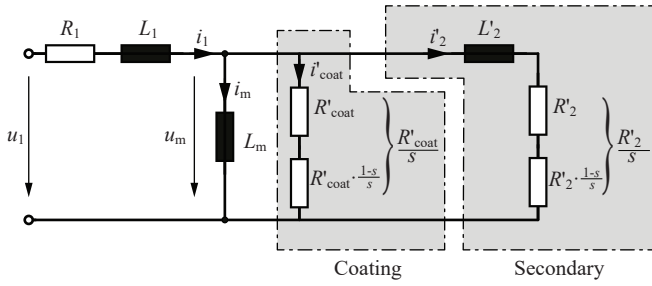


Fig. 2. The equivalent circuit of an induction machine, extended by an additional branch for the secondary coating, is used to characterize the electric behavior of a SLIM.

practical realization of the later described test setup is also realized accordingly.

A. Equivalent Circuit

The equivalent circuit of an induction machine with an addition on the secondary side (cf. Fig. 2), accounting for the conductive coating is used for general considerations on the performance of the SLIM. As a remark, it should be mentioned that the equivalent circuit represents the behavior of one phase (of a m -phase system) with respect to the star point. Secondary quantities are transformed to the primary side and marked with an apostrophe ($'$).

B. Stator Modeling

Derived from Pouillet's law, the stator coil resistance R_1 can be expressed as

$$R_1 = \frac{l_{\text{wire}}}{\kappa_{\text{Cu}} A_{\text{wire}}} = p N^2 \frac{2(l_x + l_y + l_{\text{end}})}{\kappa_{\text{Cu}} A_{\text{slot}} k_f} \quad (1)$$

as a function of wire length l_{wire} , its conductivity κ_{Cu} and the conducting cross section A_{wire} . It is also stated as function of the stator geometry parameters: number of pole pairs p , number of turns N , coil span l_x , stator transversal length l_y , additional wire length for the end windings l_{end} , slot cross section A_{slot} and copper filling factor k_f . No skin and proximity effects are included in the equation since they can be neglected for the considered operating frequency of ≈ 250 Hz, wire diameters of < 2 mm and low slot leakage field (confirmed with FEM below). A too high R_1 leads to high losses in the stator windings and prevents any electrical power to be harvested by the machine. Hence, it is an important aspect determining the efficiency for EH.

The primary stray inductance L_1 can be obtained with an analytic stray path calculation [27], a FEM simulation or with measurements. The primary stray inductance causes an inductive voltage drop; however, since the energy harvester is driven with constant current amplitude, and the voltage utilization of the power semiconductors of the inverter stage connected to the stator windings is not a primary concern, L_1 is not discussed further.

Furthermore, stator core losses are omitted in the equivalent circuit, since the stator is made of laminated steel M235-35, and for the geometries and operating conditions specified later, the loss model from [28] predicts the core losses to be less than 10% of the copper losses.

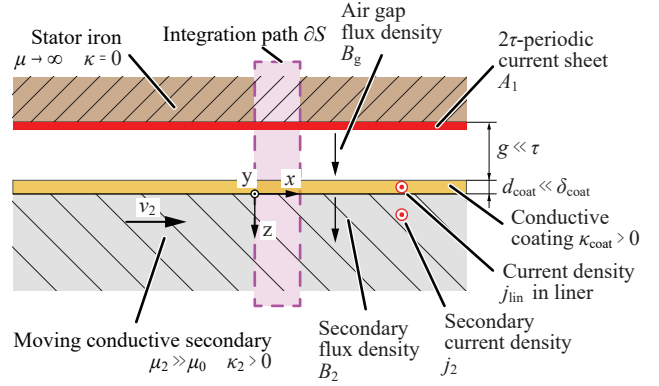


Fig. 3. Idealized 2-D model of a SLIM with solid steel secondary and a thin conductive coating for deriving the equivalent circuit elements.

C. Modeling of Main and Secondary Impedances

As already stated, the induced current and the magnetic field in the secondary are not guided in dedicated paths as e.g. in a squirrel-cage rotating induction machine. In contrast, their distribution is the solution of an electromagnetic field problem, which shall be briefly analyzed below. Fig. 3 shows the simplified geometric parameters as well as all physical quantities for deriving the secondary equivalent circuit elements according to Fig. 2. It is derived for an ideal machine, which is endlessly extended in x - and y - directions, according to Fig. 3.

For inducing current in the secondary matter, clearly, the stator field must have a different speed than the speed v_2 of the moving conductive secondary. For consistency with rotating machine theory, the frequency of fields apparent in the secondary matter is

$$\omega_2 = s \omega_1, \quad (2)$$

where s is the slip and ω_1 the frequency of electric quantities in the stator.

The flux density in the air gap can then be assumed as

$$\vec{B}_g(t) = \begin{pmatrix} B_{g,x} \\ B_{g,z} \end{pmatrix} = \begin{pmatrix} 0 \\ \hat{B}_g \cdot \sin(\pi/\tau x + \omega_1 t) \end{pmatrix}, \quad (3)$$

and due to the condition

$$d_{\text{coat}} \ll \delta_{\text{coat}} = \sqrt{\frac{2}{|\omega_2| \cdot \mu_{\text{coat}} \cdot \kappa_{\text{coat}}}}, \quad (4)$$

which requires that the conductive coating on the secondary's surface is sufficiently thinner than the skin depth in the coating material, the flux density in the coating material is also \vec{B}_g .

The fundamental equation for solving the field distribution problem in the secondary is

$$\nabla \times (\nabla \times \vec{B}_2) = -\mu_2 \cdot \kappa_2 \cdot \frac{\partial \vec{B}_2}{\partial t}, \quad (5)$$

which is derived from Maxwell's equations.

Defining the flux density in the secondary \vec{B}_2 as the real part of an exponential function with complex eigenvalue \underline{s}_B as

$$\vec{B}_2(t) = \text{Re} \left\{ \underline{\vec{B}}_2 \cdot \exp \left(\underline{s}_B^T \cdot \begin{pmatrix} x \\ z \\ t \end{pmatrix} \right) \right\}, \quad (6)$$

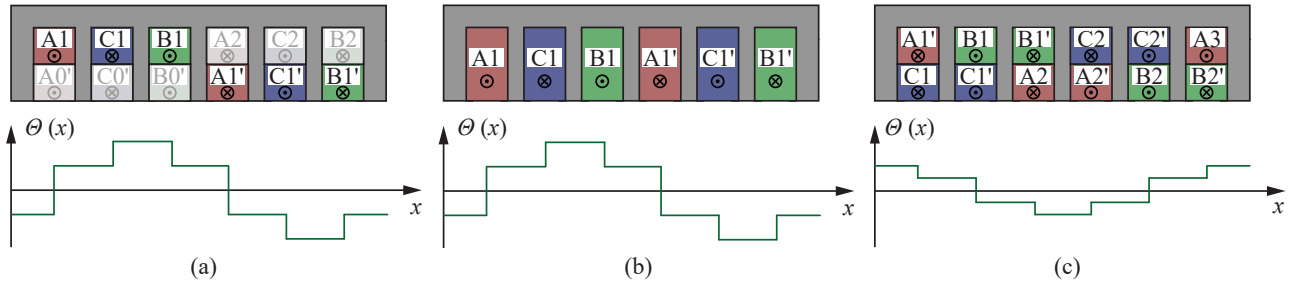


Fig. 4. Winding schemes and their respective excitation field distribution under investigation for the SLIM. For the excitation field plot, $i_b = i_c = -1/2i_a$ is assumed. (a) Typically used distributed two-layer winding for rotating machines or long SLIMs. In a SLIM, the first 3 and last 3 slots are only half filled. (b) One-layer distributed winding. Manufacturing of end windings is challenging due to intersection of the phases. (c) Concentrated two-layer winding scheme, generating a similar excitation field distribution.

further non-ideal effects (e.g. due to the large hysteresis of the considered secondary material) into account.

Finally, the harvested power on the machine's terminal P_1 can be found as

$$P_1 \approx -k \cdot p l_y \tau^{3/2} v_2^{3/2} \cdot \underbrace{\frac{(m N \xi I_1)^2}{(g + d_{\text{coat}})^2} \cdot \left(\sqrt{\frac{\kappa_2}{\mu_2}} + \sqrt{\frac{\pi}{\tau}} v_2 \kappa_{\text{coat}} d_{\text{coat}} \right)}_{P_2} + \underbrace{m R_1 I_1^2}_{P_{\text{cu}}} \quad (19)$$

which describes the scaling of the harvested power with respect to geometric and material parameters. Beneficially, nonideal effects and losses in the system, except for primary copper losses, scale with the extracted power from the secondary P_2 . As described previously, stator iron losses are negligible compared to copper losses and therefore disregarded in the scaling law. With (19), one can quantify the two opposing effects on harvested power with increasing coating thickness d_{coat} . Increased magnetic air gap counteracts the positive effect of providing a low impedance path for induced currents. Therefore, an optimal coating thickness can be calculated.

IV. WINDING SCHEME FOR A SHORT SLIM ENERGY HARVESTER

Clearly, a SLIM for EH should feature a compact design and low stator losses. Starting from an analytic consideration of the harvested power (19), two SLIM prototypes with large pole pitch τ and rather short transversal length are investigated. Typically, in rotational induction machines, distributed windings according to or similar to winding scheme Fig. 4a are realized. It is a two-layer winding and one coil has one side (cf. Fig. 4a A1) in the inner layer and one coil side (cf. Fig. 4a A1') in the outer layer. This ensures that although the winding scheme is a distributed one, the end windings do not intersect. Consequently, for a linear induction machine with this scheme, the first and the last three slots would only be half filled (cf. Fig. 3 of [23]). Only for long linear induction machines ($p > 5$) as e.g. used traction applications, the number of half-filled slots is acceptable.

Essential for the operation of an induction machine is a relatively smooth excitation field distribution. In this study,

only winding schemes with similar excitation field shape (cf. lower part of Fig. 4) with a total harmonic distortion (THD) of 6.9%, namely Fig. 4b and Fig. 4c are considered. For the ease of manufacturing, well-known methods for improving the sinusoidal shape of the excitation field distribution as fractional pitching are not investigated further in this study.

The winding scheme shown in Fig. 4b is distributed and can be realized for $p = 1$, but the end windings intersect. Winding scheme of Fig. 4c has concentrated windings, which lead to short end windings, beneficial properties in the manufacturing process and typically higher copper filling factor than Fig. 4b. It should be denoted that phases B and C have $2p$ coils, while phase A has $2p + 1$ coils in a practical realization. A drawback of the winding scheme in Fig. 4c is the reduced excitation field amplitude due to excitation cancellation across different phases in one slot. With (1), for the same excitation field amplitude, the following copper loss ratio between winding schemes of Fig. 4b and Fig. 4c can be deducted

$$\frac{P_{\text{cu,conc}}}{P_{\text{cu,dist}}} \approx \frac{4(\tau/3 + l_y) k_{f,\text{dist}}}{(\tau + l_y) k_{f,\text{conc}}} \approx 2, \quad (20)$$

where $\tau \approx l_y$ is assumed for the SLIM prototypes and $k_{f,\text{conc}} = 0.27$, $k_{f,\text{dist}} = 0.33$ were obtained by manufactured prototype windings. Therefore, the winding scheme of Fig. 4b was implemented as it shows about half the stator copper losses, compared to the winding scheme of Fig. 4c.

V. FEM AND EXPERIMENTAL RESULTS ON EH OPERATION

Presented experimental results were obtained with the test setup of Fig. 5. Results of time-transient FEM simulations are provided to further investigate the device in operation and demonstrate that the analytic model, simulations and measurement results agree.

The secondary wheel in Fig. 5 is driven with an off-the-shelf induction machine and a variable speed drive. A torque sensor (type Burster 8661-5050-1210 with ± 10 mNm accuracy) provides an accurate measurement of the secondary rotational speed and the torque on the drive shaft. The SLIM prototype under test is mounted on a positioning table with a rigid arm. In the measurements presented in this work, the SLIM is driven with an adjustable three-phase AC voltage source "Elgar SW 5250 A". All phase currents, phase-to-star

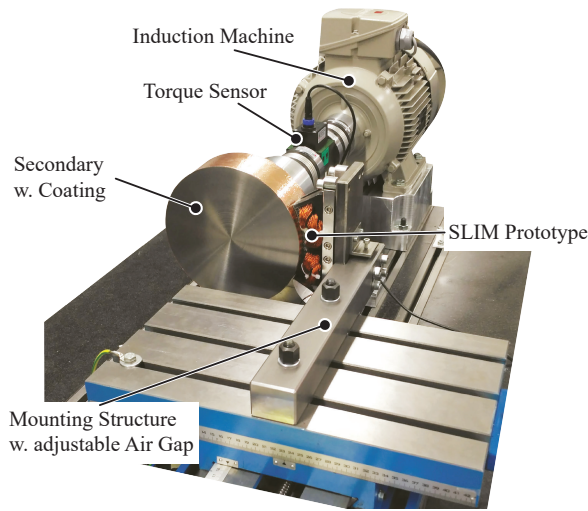


Fig. 5. Setup for conducting measurements on EH with SLIMs. The SLIM under test (A2 cf. Table I shown) is mounted on a positioning stage with a rigid arm. The replaceable secondary wheel ($d_2 = 200$ mm) is driven by a commercial induction machine with variable speed drive.

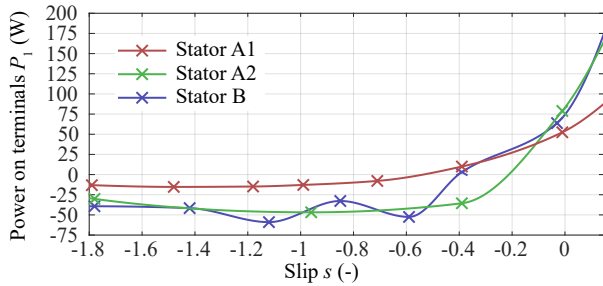


Fig. 6. Power P_1 measurement results for the stator prototypes according to Table I in generator operation. The end effects, which cause the measured power curve to show several local minima, are more pronounced with stator B than with A1 and A2. Power in the 10-watt range can be extracted on the machines' terminals and show the EH capability of the concept. The maximum power point (MPP) in slip for EH is $s \approx -1$ for all tested prototypes.

point voltages, active and apparent power of the SLIM on the machines' terminals P_1 are measured with a precision power analyzer "Norma D6100".

A. Generator Operation

Fig. 6 shows measurement results of the manufactured SLIM prototypes in generator operation. Measurements are for $g = 0.5$ mm air gap and constant RMS current. The current in stators A1 and A2 was set to $I_1 = 2$ A and with stator B to $I_1 = 8$ A, such that a similar current density in the winding of $S = 3.8$ A/mm² is present. The secondary surface speed was set to $v_2 = 29$ m/s. Although the tested prototypes are comparably short in length (pole pair number of 1 and 2), significant power can be extracted. The maximum power point in terms of slip is around $s = -1$ for all three tested machine prototypes. End effects, which cause the measured power curve to show several local minima are most pronounced with stator B. Reference [31] discusses the origin of rippled output power and thrust due to end effects in SLIMs.

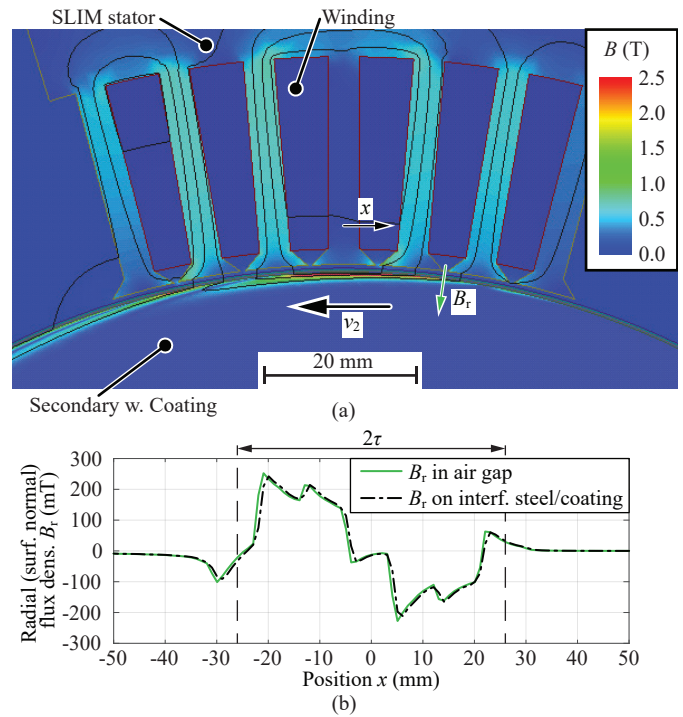


Fig. 7. 2-D FEM simulation of stator A1 according to Table I in generator operation with two layers of copper coating, $s = -1.18$, $v_2 = 29$ m/s and $I_1 = 2$ A. It can be observed in (a) that the flux in the secondary concentrates close to the surface. Stator teeth do not saturate and the flux density in the winding window is low. (b) Radial component (normal to the surface) of the flux density in the air gap and on the interface between coating and steel wheel.

TABLE I
PARAMETERS OF THE SLIM HARVESTERS.

Parameter	Var.	A1	A2	B
Stator material		M235-35A		
Pole pitch	τ	26 mm		52 mm
Stator width	l_y	30 mm		45 mm
No. of pole p.	p	1	2	1
Opt. No. of coat. layers	N_{coat}	2	3	1
No. of phases	m	3		
Winding window	A_{slot}	165 mm ²		267 mm ²
Cu filling factor	k_f	0.274		0.234
Number of turns	N	90		30
Wire gauge		AWG 20		AWG 14
Winding factor	ξ	1		
Stat. winding resist.	R_1	0.635 Ω	1.27 Ω	0.081 Ω
Stat. stray induct.	L_1	2.47 mH	4.93 mH	0.428 mH
Sec. diameter	d_2	200 mm		
Sec. ax. length	$l_{y,2}$	60 mm		

Fig. 7 shows simulation results in terms of the flux density distribution for stator A1 according to Table I in generator operation. It can be observed that flux density in the secondary is concentrated in a small sheet on the rotor's surface due to the skin depth. Moreover, it can be observed that the stator is magnetically well-dimensioned as the stator teeth are not saturating and the flux density in the winding window is low. Therefore, the initially taken assumption that stator iron losses and the winding's proximity losses are low and therefore disregarded in the power scaling law is valid.

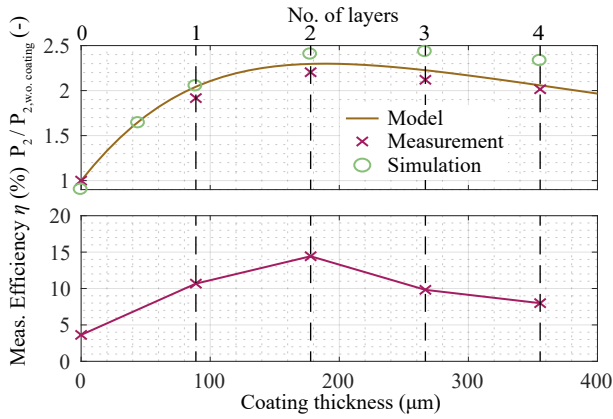


Fig. 8. Impact of secondary coating on the harvested power and overall shaft-to-machine-terminals efficiency. Results are for stator A, $I_1 = 2$ A, secondary material C45E, tip speed of $v_2 = 29$ m/s and MPP in slip. The air gap between stator and secondary wheel or coating surface, respectively, was set to $g_m = 0.5$ mm.

TABLE II
PARAMETERS FOR SCALING LAW CONFIRMATION.

Parameter	Var.	Value
Stator		A2
Stator current	I_1	4 A
Air gap	g	0.5 mm
Carter factor	k_c	1.6
S235 Permeability	μ_{S235}	1100 μ_0
C45E Permeability	μ_{C45E}	550 μ_0
S235 Conductivity	κ_2	5.67 MS/m
C45E Conductivity	κ_2	4.97 MS/m
Obtained Scaling Parameter	k	$2 \cdot 10^{-14} \frac{\text{kg}^2 \cdot \text{m}^2}{\text{s}^4 \cdot \text{A}^4}$

B. Optimal copper coating thickness

As discussed in Sec. III, an optimal value for coating thickness on the secondary exists. Therefore, in Fig. 8 the stated analytical model is verified with FEM simulation results and measurements. The SLIM prototype A1 operating in maximum power point (MPP) with a C45E secondary and copper coating is considered. The maximum power point was obtained in a grid search over excitation frequency f_1 . The coating was applied in form of an adhesive copper foil tape [33] with electrically conductive adhesive. In order to take the effect of the adhesive into account, an averaged conductivity of $\kappa_{\text{coat}} = 23$ MS/m is applied in the models.

In the top plot of Fig. 8, which shows the increase in harvested power, measurement results and FEM simulations agree well with the model according to (18). For stator A1, the EH performance can be improved by a factor of 2. Measurement results in Fig. 8 of the overall shaft-to-machine-terminals efficiency that the efficiency can be improved by a factor of 3 due to copper coating. The positive effect of the introduced low-impedance path for eddy currents predominates over the negative effect of increased magnetic air gap. The optimum was found with two layers of adhesive copper foil tape [33] (total coating thickness $d_{\text{coat}} \approx 180$ μm). With more than two layers of coating on the secondary, the effect of increased magnetic air gap dominates and the extracted power decreases.

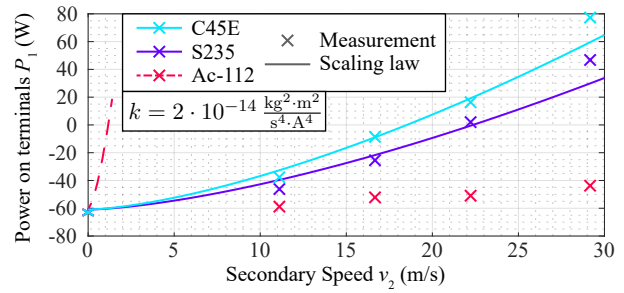


Fig. 9. Power P_1 measurement results for stator prototype A2 and different secondaries (without coating) over a secondary speed range. In accordance to the models, best EH performance was achieved with steel C45E. The analytical model is only suitable for ferromagnetic secondaries (under the considered operating conditions) and therefore model and measurements disagree for an aluminum Ac-112 secondary.

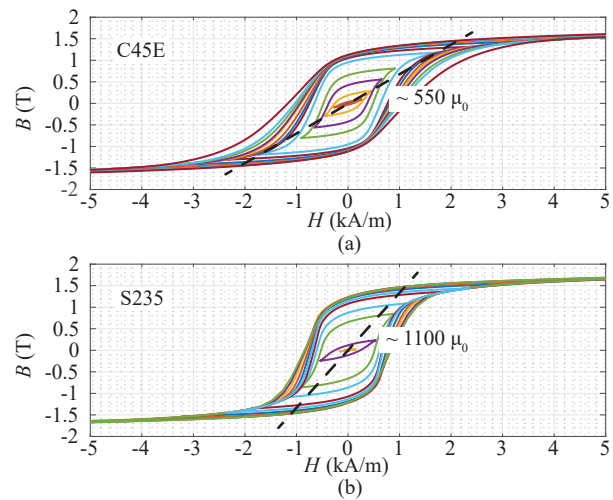


Fig. 10. B-H curves of secondary material steels C45E (in (a); cf. [34]) and S235 (in (b)). Measurements in (b) were conducted electrically on a ring specimen at $f = 1$ Hz. Dashed lines show the linearized permeability for an excitation amplitude of $B_{pk} = 1.5$ T, which is used in the scaling law.

C. Scaling law and impact of secondary material

Fig. 9 shows the validity and limitation of the presented analytical model i.e. scaling law (cf. (19)). Different secondary material configurations according to their performance in EH are analyzed. Parameters for this analysis are summarized in Table II. In accordance with (19), the secondary conductivity and permeability are characterizing the performance of a secondary. Hence, aluminum should show best power extraction capabilities as the conductivity is high ($\kappa_{2,Ac-112} = 35$ MS/m; approx. 7-times higher than in steel) and the permeability low ($\mu_{2,Ac-112} \approx \mu_0$). In the measurements, this cannot be confirmed and it clearly shows that condition (7) is necessary. Ferromagnetic and conductive secondaries (C45E, S235) fulfill this condition with ease. However, it is only fulfilled for high speeds ($v_2 > 100$ m/s) with aluminum secondaries [35]. Hence, the derived model/scaling law is not suitable for the Ac-112 secondary under the given operating conditions. In the authors' opinion, a disagreement of model and measurements in this case is of minor concern as measurement results show

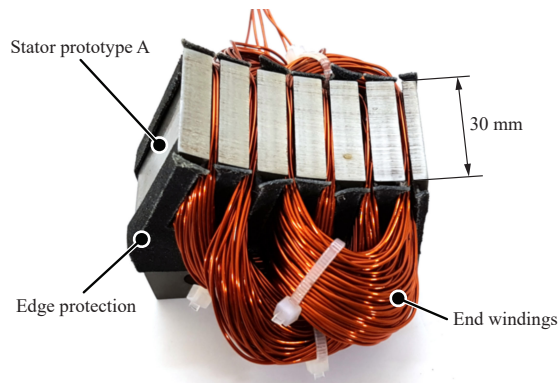


Fig. 11. Photograph of manufactured stator A.

that a non-ferromagnetic secondary performs poorly in energy harvesting (i.e. no energy can be harvested).

B-H curve measurements of secondary materials C45E and S235 are shown in Fig. 10. From the measured B-H curves, a linear permeability μ_2 was fit for an excitation amplitude of $B_{pk} = 1.5$ T and also given in Fig. 10. Moreover, electric conductivities of these materials were measured on cylindrical specimen and are given in Table II.

Crosses in Fig. 9 show measurements of the harvested power and solid lines the scaling law with the scaling coefficient k according to Table II. The scaling coefficient was fitted on the measurement data provided for S235 and C45E in Fig. 9. For the S235 and C45E secondary, measurements and scaling law agree well. Higher speed leads to reduced skin depth and higher flux density in the secondary material. Furthermore, the secondary materials' B-H curves (cf. Fig. 10) show strong non-linearity and saturation. Hence, for measurement points in Fig. 9 with $v_2 = 29$ m/s, the scaling law (where constant μ_2 was assumed) slightly underestimates the measured power. Finally, C45E is superior to other tested secondary materials for EH and all further measurements are with a C45E secondary.

VI. CASE STUDY ON SLIM ENERGY HARVESTER

In this section, a case study of a SLIM energy harvester, depicted in Fig. 11, with $P_1 = 15$ W power output and 16.5 cm^2 area coverage, suitable for EH from a rotating shaft is presented. Furthermore, a scheme for reactive power compensation is discussed. Table III details the specifications of the harvester and the analyzed operation point.

In Fig. 12, the voltage and current phasors are given for power extraction of 15 W including reactive power compensation using three EPCOS B32524 $68\ \mu\text{F}$ film capacitors, according to Fig. 13. The measured voltages and currents as a function of time are depicted in Fig. 14 for the operation with and without compensation, respectively. The asymmetric operation of the SLIM is clearly visible, which can be explained by the (static) end effects. Phases A and C harvest power whereas phase B is drawing power. Therefore, a unity power factor cannot be reached, even with capacitive compensation. The apparent power can be reduced from $S = 108$ VA to $S = 34$ VA, which corresponds to a power factor of $\lambda = 0.44$. Hence, the required apparent power needed from the supplying AC voltage and/or inverter stage is reduced by a factor of three,

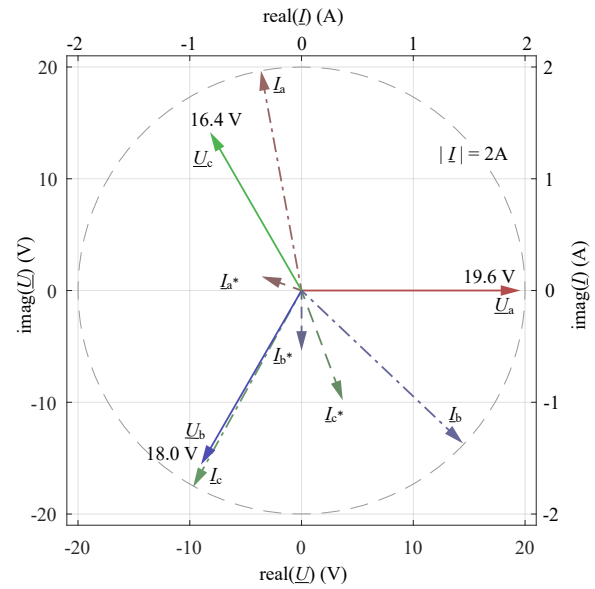


Fig. 12. Voltages and currents pointer diagram showing the currents through the machine's terminals and after compensation, flowing through the driving AC voltage sources. Labels are according to schematic Fig. 13.

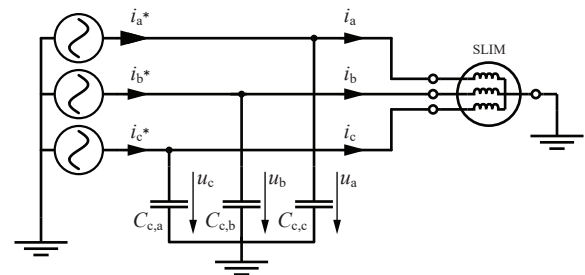


Fig. 13. Schematic for reactive power compensation. The SLIM is driven with a three-phase controllable voltage source and adjusted such that the RMS value of the machine's phase currents are equal. The bank of reactive power compensation capacitors is connected in parallel to the machine's phases.

which leads to a lower rated power of the inverter and/or to a reduction of losses.

For the conducted measurements, a controlled three-phase voltage source ("Elgar SW 5250 A") was utilized for driving the SLIM. In this setup, parallel compensation of reactive power is favorable as it still guarantees well-defined terminal voltages on the SLIM's electric terminals and hence, a well defined moving air gap flux vector. Series compensation of reactive power might be favorable, when operating the SLIM in an EH environment with a switched-mode drive, but requires (conversely to the parallel compensation) higher bandwidth current control.

VII. CONCLUSION

With today's megatrends such as ubiquitous computing and the Internet of Things (IoT) more and more remote systems are being digitalized and connected. This requires a new generation of modular, robust, and low-cost energy harvesters

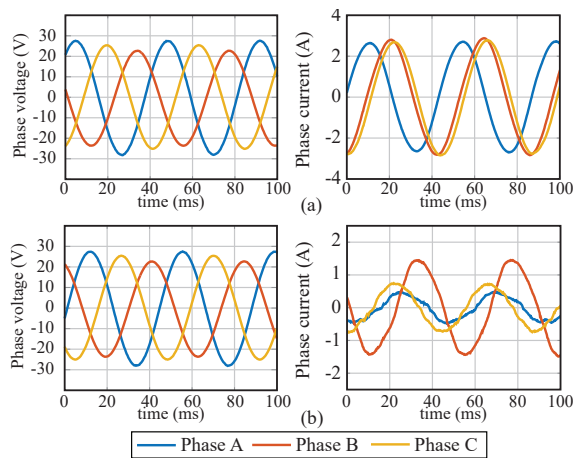


Fig. 14. Measured phase currents and phase-to-star point voltages without (a) and with compensation (b).

TABLE III
 SPECIFICATIONS OF HARVESTER CASE STUDY.

Parameter	Variable	Value
Measured air gap	g_m	0.5 mm
Stator material		M235-35A
Secondary material		Steel C45E
No. of coating layers		2
Tot. coating thickness	d_{coat}	180 μ m
Secondary surface speed	v_2	29 m/s
Stator phase current (RMS)	I_1	2 A
Excitation frequency	f_1	230 Hz
Apparent power on SLIM	S_1	108 VA
Apparent power on drive	S_{drive}	34 VA
Active power on SLIM	P_1	14.8 W
SLIM efficiency	η	14 %

for powering an increasing variety of electrical loads with growing power requirements. In this work, such an energy harvester is proposed by placing the stator of a single-sided linear induction machine (SLIM) close to a moving, solid conductive body, which exists in the vicinity of the load to be powered. The SLIM is operated in generator mode, harvesting electrical energy from the kinetic energy of the moving body.

The applicability of a SLIM for energy harvesting (EH) is analyzed starting from a simple, yet powerful analytical model. The derived power scaling relations (17), (18) and (19) reveal the influence of geometric, electric and material parameters on the harvesting performance.

Different winding schemes that are particularly suited for EH (short SLIMs with low number of poles) are evaluated. A one-layer distributed winding scheme shows best results in the comparison and is implemented on the prototypes. The analytical model is used to find the optimum copper coating thickness. An output power increase above 100% with ≈ 0.2 mm coating thickness is predicted by the models and confirmed with measurements. Measurements with secondaries made of two different common steel grades, S235 (construction steel) and C45E (commonly used for shafts in machinery), and one aluminum alloy (Ac-112) reveal that the extracted power is increased with steel of higher carbon content (C45E). Measurements with a compact prototype, utilizing approximately 17 cm² of secondary surface area,

with optimized secondary copper layer thickness, show that harvesting 15 W of electrical power with 14% efficiency over an air gap of 0.5 mm from a secondary with tip speed of 29 m/s is possible. Energy efficiency of the system is not a primary concern (which is the typical approach in the domain of EH) as it supplies electric power at a place, where no other power supply alternative exists.

Further measurements with parallel compensation of the reactive power lead to a reduction in apparent power from 108 VA to 34 VA. Due to imbalances in harvested power across the phases, which is a well-known phenomenon for short SLIMs, the power factor after compensation does not reach unity.

In summary, this paper shows that EH with a SLIM in the watt range from a moving steel body with copper coating is feasible for higher speeds (29 m/s) and low air gap (0.5 mm). For applications with different requirements, the power output can be estimated by a derived and verified scaling law.

ACKNOWLEDGMENT

The authors would like to express their sincere appreciation to Nabtesco Corp., Japan, for the financial and technical support of research on EH technologies at the Power Electronic Systems Laboratory, ETH Zurich, which provided the basis for achieving the results presented in this paper. In particular, inspiring technical discussions with K. Nakamura, Y. Tsukada and Y. Ono are acknowledged.

REFERENCES

- [1] Y. K. Tan and S. K. Panda, "Energy harvesting from hybrid indoor ambient light and thermal energy sources for enhanced performance of wireless sensor nodes," *IEEE Trans. Ind. Electron.*, vol. 58, no. 9, pp. 4424–4435, Sep. 2011.
- [2] A. Khaligh, P. Zeng, and C. Zheng, "Kinetic energy harvesting using piezoelectric and electromagnetic technologies -state of the art," *IEEE Trans. Ind. Electron.*, vol. 57, no. 3, pp. 850–860, Mar. 2010.
- [3] Z. Wang, J. Hu, J. Han, G. Zhao, J. He, and S. X. Wang, "A novel high-performance energy harvester based on nonlinear resonance for scavenging power-frequency magnetic energy," *IEEE Trans. Ind. Electron.*, vol. 64, no. 8, pp. 6556–6564, Aug. 2017.
- [4] M. R. Elhebeary, M. A. A. Ibrahim, M. M. Aboudina, and A. N. Mo-hieldin, "Dual-source self-start high-efficiency microscale smart energy harvesting system for iot," *IEEE Trans. Ind. Electron.*, vol. 65, no. 1, pp. 342–351, Jan. 2018.
- [5] R. J. M. Vullers, R. v. Schaijk, H. J. Visser, J. Penders, and C. V. Hoof, "Energy harvesting for autonomous wireless sensor networks," *IEEE Solid-State Circuits Mag.*, vol. 2, no. 2, pp. 29–38, Jun. 2010.
- [6] J. A. R. Azevedo and F. E. S. Santos, "Energy harvesting from wind and water for autonomous wireless sensor nodes," *IET Circuits, Devices Systems*, vol. 6, no. 6, pp. 413–420, Nov. 2012.
- [7] M. Flankl, A. Tüysüz, I. Subotic, and J. W. Kolar, "Novel contactless axial-flux permanent-magnet electromechanical energy harvester," in *Proc. Conf. Expo. Applied Power Electron. (APEC)*, pp. 623–630, Mar. 2016.
- [8] I. Boldea, L. Tutelea, W. Xu, and M. Pucci, "Linear electric machines, drives and maglevs: an overview," *IEEE Trans. Ind. Electron.*, Jul. 2017.
- [9] G. Lv, D. Zeng, T. Zhou, and Z. Liu, "Investigation of forces and secondary losses in linear induction motor with the solid and laminated back iron secondary for metro," *IEEE Trans. Ind. Electron.*, vol. 64, no. 6, pp. 4382–4390, Jun. 2017.
- [10] T. C. Wang, "Linear induction motor for high-speed ground transportation," *IEEE Trans. Ind. Gen. Appl.*, no. 5, pp. 632–642, Sep. 1971.
- [11] J. Stickler, "A study of single-sided linear induction motor performance with solid iron secondaries," *IEEE Trans. Veh. Technol.*, vol. 31, no. 2, pp. 107–112, May. 1982.
- [12] Y. Yasuda, M. Fujino, M. Tanaka, and S. Ishimoto, "The first HSST maglev commercial train in Japan," in *Proc. Int. Conf. Magnetically Levitated Systems and Linear Drives (MAGLEV)*, pp. 76–85, Oct. 2004.

- [13] Y. Nozaki, T. Koseki, and E. Masada, "Analysis of linear induction motors for HSSST and linear metro using finite difference method," in *Proc. Int. Symp. Linear Drives for Industry Applications (LDIA)*, pp. 168–171, Sep. 2005.
- [14] J. F. Gieras, *Linear induction drives*. Oxford University Press, 1994.
- [15] E. Bolte, "Dreidimensionale Berechnung des asynchronen Sektormotors mit massivem Rotor (in German)," Ph.D. dissertation, Universität Dortmund, 1979.
- [16] W. Xu, J. Zhu, Y. Zhang, D. Dorrell, and Y. Guo, "Electromagnetic optimal design of a linear induction motor in linear metro," in *Proc. 36th Annu. Conf. IEEE Industrial Electronics (IECON)*, pp. 3067–3072, Nov. 2010.
- [17] M. Flankl, A. Tüysüz, and J. W. Kolar, "Analysis and power scaling of a single-sided linear induction machine for energy harvesting," in *Proc. 41st Annu. Conf. IEEE Industrial Electronics (IECON)*, pp. 835–842, Nov. 2015.
- [18] T. Hupponen, "High-speed solid-rotor induction machine - electromagnetic calculation and design," Ph.D. dissertation, Lappeenranta University of Technology, 2004.
- [19] European Committee for Standardization, *Steels for quenching and tempering*, Std. EN 10 083-1, 2006.
- [20] European Committee for Standardization, *Hot rolled products of structural steels*, Std. EN 10 025-2, 2005.
- [21] European Committee for Standardization, *Aluminium and aluminium alloys. Chemical composition and form of wrought products. Chemical composition and form of products*, Std. EN 573-3, 2013.
- [22] J. F. Gieras, *Handbook of electric motors*, ch. 4.6.2.4 Rotors with conductive layers, p. 273. Marcel Dekker, New York, 2004.
- [23] W. Xu, J. G. Zhu, Y. Zhang, Z. Li, Y. Li, Y. Wang, Y. Guo, and Y. Li, "Equivalent circuits for single-sided linear induction motors," *IEEE Trans. Ind. Appl.*, vol. 46, no. 6, pp. 2410–2423, Sep. 2010.
- [24] W. Xu, J. G. Zhu, Y. Zhang, Y. Li, Y. Wang, and Y. Guo, "An improved equivalent circuit model of a single-sided linear induction motor," *IEEE Trans. Veh. Technol.*, vol. 59, no. 5, pp. 2277–2289, Jun. 2010.
- [25] R. C. Crepe, J. A. C. Ulson, and J. F. Rodrigues, "Influence of design parameters on linear induction motor end effect," *IEEE Trans. Energy Convers.*, vol. 23, no. 2, pp. 358–362, Jun. 2008.
- [26] J. F. Gieras, G. E. Dawson, and A. R. Eastham, "A new longitudinal end effect factor for linear induction motors," *IEEE Trans. Energy Convers.*, vol. EC-2, no. 1, pp. 152–159, Mar. 1987.
- [27] V. D. Nene, *Handbook of electric motors*, ch. 4.5.4.3 Stator slot leakage reactance, pp. 268–269. Marcel Dekker, New York, 2004.
- [28] M. Flankl, A. Tüysüz, and J. W. Kolar, "Cogging torque shape optimization of an integrated generator for electromechanical energy harvesting," *IEEE Trans. Ind. Electron.*, vol. 64, no. 12, pp. 9806–9814, Dec. 2017.
- [29] W. Soong, "Sizing of electrical machines," *Power Engineering Briefing Note Series*, vol. 9, pp. 17–18, Sept. 2008.
- [30] J. C. H. Bone, "Influence of rotor diameter and length on the rating of induction motors," *IEE Elect. Power App.*, vol. 1, no. 1, pp. 2–6, Feb. 1978.
- [31] S. Yamamura, H. Ito, and Y. Ishulawa, "Theories of the linear, induction motor and compensated linear induction motor," *IEEE Trans. Power App. Syst.*, vol. PAS-91, no. 4, pp. 1700–1710, Jul. 1972.
- [32] H. Bolton, "Transverse edge effect in sheet-rotor induction motors," *Proc. IEE*, vol. 116, no. 5, pp. 725–731, May. 1969.
- [33] 3M. Copper foil tape 1126 datasheet. (2014, May). [Online]. Available: <http://multimedia.3m.com/mws/media/1043610/tape-1126-copper-foil-with-conductive-adhesive.pdf>
- [34] M. Flankl, A. Tüysüz, and J. W. Kolar, "Impact of iron dust on electromechanical systems: A case study," in *Proc. 2nd Annu. Conf. IEEE Southern Power Electronics (SPEC)*, pp. 1–8, Dec. 2016.
- [35] M. Flankl, T. Wellerdieck, A. Tüysüz, and J. W. Kolar, "Scaling laws for electrodynamic suspension in high-speed transportation," *IET Electric Pow. Appl.*, vol. 12, pp. 357–364, Mar. 2018.



Michael Flankl (S'12) received his BSc degree in Mechatronics from JKU Linz, Austria in 2012. From 2010 to 2012 he was a freelancer at the electrical engineering / electronics department of Engineering Center Steyr GmbH (branch of Magna Powertrain), St. Valentin, Austria. He has received the MSc degree in Robotics, Systems & Control from the Swiss Federal Institute of Technology (ETH) Zurich in 2014. Since May 2014, he is a PhD candidate at the Power Electronic Systems Laboratory at ETH Zurich. He is supervised by Prof. Johann W. Kolar and working on electrodynamic energy harvesting from moving conductive surfaces. His research interests and professional experience include special electric machines, drives, railway and automotive transportation systems as well as optimization and control thereof.



Lucas de Oliveira Baumann (S'16) received the B.Sc. degree in electrical engineering and information technology from ETH Zurich, Switzerland, in 2017. Since 2017, he has been working toward the M.Sc. degree in electrical engineering and information technology at ETH Zurich. His areas of interest include power electronics, control and electrical machines.



Arda Tüysüz (S'10 - M'13) received his B.Sc. degree in electrical engineering from Istanbul Technical University, Istanbul, Turkey, in 2006, his M.Sc. degree in electrical power engineering from RWTH Aachen University, Aachen, Germany, in 2009, and his Ph.D. degree in electrical drives from the Swiss Federal Institute of Technology (ETH) Zurich, Zurich, Switzerland, in 2015. After obtaining his Ph.D. degree, he worked until September 2017 as a Post-Doctoral Researcher with the Power Electronic Systems Laboratory of ETH Zurich. His research interests during this period included novel electrical machine topologies, self-sensing control of high-speed electrical machines, electrical drives with very high signal-to-noise ratio and wide-bandgap power devices for very efficient and compact electrical drive systems. He is currently with the ABB Corporate Research Center in Ladenburg, Germany.



Johann W. Kolar (M'89-SM'04-F'10) is a Fellow of the IEEE and received his Ph.D. degree (summa cum laude) from the Vienna University of Technology, Austria in 1999. He is currently a Full Professor and the Head of the Power Electronic Systems Laboratory at the Swiss Federal Institute of Technology (ETH) Zurich. He has proposed numerous novel PWM converter topologies, and modulation and control concepts and has supervised over 60 Ph.D. students. He has published over 750 scientific papers in international journals and conference proceedings, 3 book chapters, and has filed more than 150 patents. He has presented over 20 educational seminars at leading international conferences, has served as IEEE PELS Distinguished Lecturer from 2012 through 2016, and has received 25 IEEE Transactions and Conference Prize Paper Awards, the 2014 IEEE Power Electronics Society R. David Middlebrook Achievement Award, the 2016 IEEE William E. Newell Power Electronics Award, the 2016 IEEE PEMC Council Award, and two ETH Zurich Golden Owl Awards for excellence in teaching. He has initiated and/or is the founder of 4 ETH Spin-off companies. The focus of his current research is on ultra-compact and ultra-efficient SiC and GaN converter systems, wireless power transfer, Solid-State Transformers, Power Supplies on Chip, as well as ultra-high speed and ultra-light weight drives, bearingless motors, and energy harvesting.